Materials Advances

ROYAL SOCIETY OF CHEMISTRY

PAPER

View Article Online
View Journal | View Issue

Cite this: *Mater. Adv.*, 2026, 7, 3339

Transition metal-embedded Nb_2S_2C as a high-performance bifunctional electrocatalyst for the OER and ORR: insights from DFT simulations

K. Simmy Joseph, [a] Brahmananda Chakraborty *[bc] and Shweta Dabhi *[a]

Received 2nd January 2026,
Accepted 5th January 2026

DOI: 10.1039/d6ma00002a

rsc.li/materials-advances

The commercialization of energy storage and conversion technologies depends on the development of effective electrocatalysts. In this study, we investigate the incorporation of transition metal (TM) dopants – platinum (Pt), copper (Cu), iridium (Ir), cadmium (Cd), and rhodium (Rh) into two-dimensional Nb_2S_2C to enhance electrocatalytic performance for the oxygen evolution reaction (OER) and oxygen reduction reaction (ORR). Density Functional Theory (DFT) calculations reveal that TM-doped Nb_2S_2C substantially lowers the overpotentials, achieving 0.32 V for the OER with Pt–Nb_2S_2C and 0.35 V for the ORR with Rh–Nb_2S_2C. Partial density of states (PDOS) analyses indicate that the TM dopant modulates the electronic structure of Nb_2S_2C, facilitating the adsorption and activation of reaction intermediates and thus improving catalytic efficiency. The OOH dissociation step is identified as the rate-determining step in the four-electron ORR pathway for Rh–Nb_2S_2C, with an activation energy of 2.25 eV. Furthermore, *ab initio* molecular dynamics (AIMD) simulations confirm the structural and thermodynamic stability of Pt- and Rh-doped Nb_2S_2C under operational conditions. These findings offer a rational strategy for designing high-performance Nb_2S_2C-based electrocatalysts and underscore the potential of Pt- and Rh-doped systems as stable and efficient catalysts for the OER and ORR in sustainable energy technologies.

1. Introduction

The contemporary energy revolution highlights the significance of clean, renewable, and high-efficiency energy technology in mitigating energy crises and environmental contamination. The OER and ORR are indispensable processes for devices such as water splitting systems, metal air batteries, and fuel cells.[1–3] However, these processes face challenges due to high energy barriers and also sluggish kinetics, hindering the transformation of electric energy. In the field of novel energy technologies, materials with the ability to effectively catalyse OER reactions have enormous potential. Platinum-based nanostructures are commonly used as catalysts to ameliorate OER, and ORR activities, but their substantial cost and limited abundance encumber their widespread commercial applications.[4] Comparing multifunctional electrocatalysts to monofunctional catalysts, which are limited to catalysing a single reaction at a time, has drawn attention to the former's streamlined procedures and higher catalytic efficiency.[5] Consequently, in order to overcome the difficulties of attaining superior catalytic performance throughout the ORR and OER for a single material, it is imperative to investigate high-performance and inexpensive multifunctional catalysts.

The newly synthesized compound Nb_2Se_2C in bulk bears resemblance to transition metal carbochalcogenides (TMCCs), which are a combination of TM carbides (MXenes) and TMDCs (transition metal dichalcogenides). A study conducted in 1990 by Braud *et al.* found that chain compounds $(CH_3)_4NMnCl_{13}$ (TMMC) and $(CH_3)_4NCdC_{13}$ (TMCC), which are produced from octahedral chain rotation, exhibit a new high-temperature orientationally disordered phase (phase I). A complicated Frenkel model describes the orientational disorder of the $(CH_3)_4N$ group (TMA) in phase I.[6] It's interesting to note that Beckmann *et al.* synthesized Ta_2S_2C, a multilayer TMCC, for the first time in early 1970.[7] Two decades later, in 1992, Boller along with Hiebl reported the synthesis of a metastable phase Nb_2S_2C with a structure resembling Ta_2S_2C by means of a topochemical reaction that began with H–Nb_2S_2C and resulted in $Cu_{0.7}Nb_2S_2C$, from which Cu was deintercalated.[8] In 2001 it was discovered that a few of these multilayered carbo-sulphides were superconductors.[9]

The tuneable electronic structures of TMDs along with MXenes have attracted much attention from material scientists

[a] *Department of Physical Science, P. D. Patel Institute of Applied Sciences, Charotar University of Science and Technology, CHARUSAT Campus, Changa, 388421, Gujarat, India. E-mail: shwetadabhi.phys@charusat.ac.in*
[b] *High Pressure and Synchrotron Radiation Physics Division, Bhabha Atomic Research Centre, Mumbai, India. E-mail: brahma@barc.gov.in*
[c] *Homi Bhabha National Institute, Mumbai, 400085, India*

in the field of electrochemistry in 2020. This new Nb_2Se_2C combination is intended to function as a material similar to "TMD–MXene." Because of its superior conductivity and enriched active sites, it performs better in the oxygen evolution reaction than the majority of previously reported TMDs, MXenes, and commercial electrocatalysts. In 2022, a close analogue of Nb_2Se_2C, single-layer Nb_2S_2C, was successfully synthesized from its multilayered crystal by electrochemical lithiation and water sonication.[10] Zhang *et al.* then investigated the 2D (two dimensional) Janus structure in 2023; this 2D material has potential applications in nanodevices. Using Nb_2S_2C, they created five stable structures by swapping out the atoms of sulfur for X atoms. The superconductivity of both structures was found to be promising, with a plausible temperature range of 1.35 to 12.66 K.[11] According to a recent study, a single Pd atom can increase catalytic activity in place of Pd metal clusters, resulting in a single-atom catalyst (SAC). Aimed at anchoring the single metal atom, the 2D material boasting a high surface-to-volume ratio shows promise because of its special qualities, which include even lattice planes with tuneable electronic states. Potential catalysts for the oxidation of carbon monoxide were investigated by Manman Li *et al.* using single atoms atop stable 2D materials. They discovered that Nb_2S_2C monolayers adorned with 3d (Fe–Zn), 4d (Ru–Cd), and 5d (Os–Hg) transition metals show promise for low-temperature CO oxidation processes. They discovered that faulty carbosulfides can serve as inexpensive and effective substrates.[12] Yeoh *et al.* optimized the catalytic activity of the ORR by means of computational screening on transition metal atoms in monolayer Nb_2S_2C. The findings demonstrated that even at high temperatures, substitutional doping *via* Ni or Rh atoms produces viable ORR catalysts that have minimal overpotentials with intact monolayer Nb_2S_2C.[13] A 2D Nb_2S_2C monolayer's potential for identifying the biomolecule catechol (Cc), potentially harmful in excess concentration, was investigated by Seetha Lakshmy *et al.* Because of orbital interactions and charge transfer, the Nb_2S_2C monolayer demonstrated higher adsorption energy of Cc and demonstrated physisorption. The investigation demonstrated the sensor's promising nature and validated its possible real-world use for Cc detection. Strong chemical binding and quick recovery were two of the improved adsorption features of the Cu-incorporated Nb_2S_2C system.[14] This discovery represents a major advancement in TMCC-based nitrobenzene detectors and advances gas sensing technologies, environmental monitoring, and safety. The ability of TMs such as Rh, Pt, Cd, Cu, and Ir to improve catalytic performance through electronic structure modulation and adsorption energy optimization of important intermediates is the basis for their selection for doping in Nb_2S_2C. While Cu and Cd aid in charge redistribution along with adsorption energy tuning, Rh, Pt, and Ir are well-known noble metals with strong activity for the OER and ORR. Structural stability is maintained by their similar ionic radii to Nb, which ensure minimal lattice distortion. Additionally, these dopants have shown catalytic effectiveness in comparable 2D materials, but it is unknown how they affect Nb_2S_2C. By methodically examining their function, this work seeks to close an important gap in expertise in the field of TM-doped Nb_2S_2C-based electrocatalysts.

The Nb–C layers are primarily responsible for the high conductivity of Nb_2S_2C, while the S layers give it enriched active sites. An exceptional electrocatalytic activity is the outcome of these characteristics. Nb_2S_2C was chosen as the substrate owing to its intrinsically stable layered framework, metallic conductivity, and robust Nb–S/C bonding network, which together offer strong and well-defined anchoring sites for transition-metal dopants. In addition, the resulting TMCC structure provides a high surface area and heteroatom-rich motifs that generate diverse adsorption environments, thereby facilitating flexible and efficient catalytic interactions. The Nb centres, with their high electronic density and accessible d orbitals, promote strong electronic coupling and optimised charge transfer with the incorporated metal atoms (Rh, Pt, Cd, Cu, Ir), ultimately tuning the overall catalytic activity. Moreover, Nb-based carbides and sulphides are widely recognised as durable and highly active supports for single-atom catalysts in various energy-conversion reactions. Collectively, these characteristics establish Nb_2S_2C as a promising and versatile platform for investigating transition-metal doping and its impact on enhancing electrocatalytic performance. However, the scientific community has not given much attention to 2D TMCCs. Motivated by the outstanding results of the ORR catalytic activity of bulk Nb_2Se_2C, we employed DFT in this work to perform a methodical analysis of the catalytic activities of the bifunctional OER, and ORR activity for pristine and single TM atom anchored on a 2D Nb_2S_2C monolayer. Adsorption energy, bonding, charge transfer, and favourable adsorption configurations are some of these findings. It has also been shown that the Pt and Rh-doped Nb_2S_2C provide the most optimal results for the ORR and OER mechanism. To the best of our knowledge, no prior reports on the OER and ORR for the 2D system Nb_2S_2C have been published as of yet.

2. Computational methods

In the context of density functional theory (DFT) simulations using the Quantum ESPRESSO package, the properties of transition metal (TM) anchored and pristine Nb_2S_2C were investigated.[15] The electron–ion interactions were modeled using plane-wave pseudopotentials, with the Perdew–Burke–Ernzerhof (PBE) functional under the generalized gradient approximation (GGA).[16] To account for long-range van der Waals interactions between Nb_2S_2C layers, the DFT-D3 method, as proposed by Grimme, was utilized. A Monkhorst–Pack *k*-point mesh of $7 \times 7 \times 1$ was applied to sample the Brillouin zone, and a convergence threshold of 10^{-6} Ry was set for geometry optimization.[17] An energy cutoff of 60 Ry was used throughout the calculations. The climbing-image nudged elastic band (CI-NEB) calculations were performed using the Quantum ESPRESSO package to determine the minimum energy pathways and reaction barriers for key steps in the OER/ORR. *Ab initio* molecular dynamics (AIMD) simulations were carried

out in VASP at 300 K for 10 ps with a time step of 1 fs to examine the thermal stability of the optimized TM@Nb_2S_2C systems.

3. Results and discussion

3.1. Structural features and OER and ORR activity of pristine Nb_2S_2C

Keeping the previously mentioned computational parameters in sight, the Nb_2S_2C supercells were made optimal by fully relaxing the atomic position with regard to cell dimension and shape by imposing a stiff vacuum level of 20 Å across the aperiodic direction. A 3 × 3 × 1 supercell of the Nb_2S_2C monolayer was created by replicating the fundamental unit cell three times in both in-plane directions (a and b). The hexagonal unit cell's calculated lattice constant for pristine Nb_2S_2C was also 9.799 Å. The supercell of pristine Nb_2S_2C, comprising 18Nb, 9C, and 18S atoms, is illustrated in Fig. 1(a and b).

To systematically determine the active adsorption sites on pristine Nb_2S_2C, we evaluated the adsorption behaviour of key OER/ORR intermediates (*O, *OH, and OOH) on all accessible surface atoms, namely Nb, S, and C. Among these, the S atoms showed the strongest affinity toward the reaction intermediates, which can be attributed to their exposed dangling bonds. Nevertheless, adsorption on Nb and C sites was also examined to verify their comparatively weak interactions and limited catalytic contribution. This comprehensive assessment clearly identifies S atoms as the dominant active centres, while Nb and C sites remain largely inactive. As a result, the pristine system provides a reliable baseline for understanding catalytic improvements induced by transition-metal doping. Consequently, all subsequent OER/ORR calculations were performed with intermediates preferentially adsorbed on S sites.

The 2D Nb_2S_2C is expected to have an elastic modulus that is more than 50% more than that of its TMDC equivalents, which are NbS_2 and TaS_2. Given its distinct composition amid two sizable categories of two-dimensional materials (MXenes along with TMDCs) and its distinctive properties derived from this composition, it is reasonable to anticipate that this family will grow quickly, even if we are reporting the first member of TMCCs here.

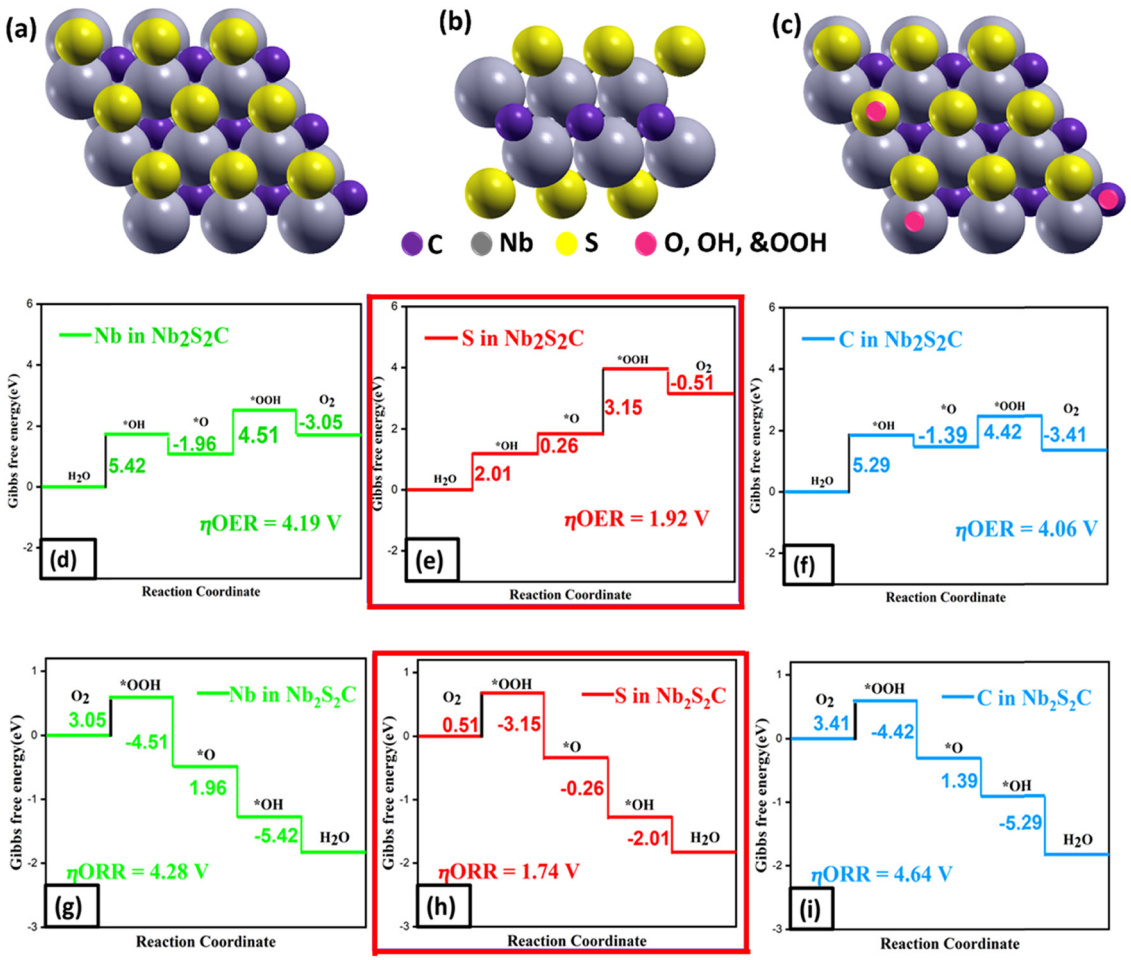

Fig. 1 (a) Top and (b) side view of the Nb_2S_2C system. (c) Schematic illustration of the Nb_2S_2C catalyst, highlighting the potential OER adsorption sites (pink circles). (d)–(f) Gibbs free-energy profiles for the OER pathways occurring on (d) Nb sites, (e) S sites, and (f) C sites within Nb_2S_2C. (g)–(i) Gibbs free-energy profiles for the ORR pathways on (g) Nb sites, (h) S sites, and (i) C sites. In all energy diagrams, the black marker denotes the rate-limiting step corresponding to the highest free-energy barrier.

We will concentrate in this section on the performance of pristine Nb_2S_2C in the other part of the water splitting, which is called the OER (the thermodynamics mechanism of the OER and ORR is in the SI).[4,18] To evaluate their effectiveness in this procedure, we have conducted calculations and analysis. Since O adsorption is not a good indicator of OER reactions, according to the literature review, we also separately investigated the whole mechanism of the OER in this work, which includes intermediates including O*, OH*, and OOH*. In pristine structures, all intermediates were made to bond to S, Nb, and C. The structure is found to be immutable after the intermediates are adsorbed, *i.e.*, the intermediates are still attached to S, Nb, and C in pristine Nb_2S_2C, respectively.

By attaching each of the O*, OH*, and OOH* species individually onto clean Nb_2S_2C surfaces, we calculated the adsorption energies of the species with geometry relaxation. One of the phases from (i)–(iv) ideally should have an energy value higher than 1.23 eV since the dissociation of water generally requires a total energy of 4.92 eV. An energy value of 1.23 eV is the ideal reaction upper limit. Yet, greater overpotentials can occur due to particular phases having higher reaction energies. A higher overpotential, however, might result from particular phases exhibiting more reaction energy. The calculated reaction energy associated with each oxygen evolution process occurring at the active sites of Nb_2S_2C is shown in Fig. 1(d, e and f). To enable comparison, the maximal reaction energies were calculated for different systems. The maximum energies associated with the following systems were determined to be 3.15, 5.29, and 5.42 eV for S, C, and Nb top in Nb_2S_2C. The kinetic transformations of the pristine Nb_2S_2C systems are as follows: Nb and C top in Nb_2S_2C (step 1: from * to OH* is phase 1), S in Nb_2S_2C (O* to OOH* is phase three). In the following ascending orders, the OER activity implies a decrease in the overpotential values: Nb, C, and S top in Nb_2S_2C. Out of all the systems, the S top in Nb_2S_2C has been demonstrated to have the highest amount of catalytic activity, with the lowest overpotential and maximal reaction energy (η_{OER} = 1.92 V).

The ORR mechanism's corresponding Gibbs free energy diagrams are shown in Fig. 1(g, h, and i). The foremost energy-intensive process for Nb top, S top, and C top in Nb_2S_2C, is the first step of O_2 with a H^+ and an e^- to produce the OOH* on the catalyst surface. The corresponding ΔG_a values for these processes are 3.05, 0.51, and 3.41 eV. It is of particular connotation that the S top in Nb_2S_2C has the lowest overpotential of 1.74 Volt for the ORR among all the adsorption sites among pristine Nb_2S_2C materials that have been examined [Fig. 1(g–i)]. Consequently, in addition, the S-top site in pristine Nb_2S_2C exhibits competent OER and ORR catalytic activity. Furthermore, the overpotentials of pristine Nb_2S_2C for the OER and ORR were computed, as shown in Fig. 1(d–i). Accordingly, the activity of the ORR increases in the following sequence: Nb in Nb_2S_2C, C in Nb_2S_2C, and S in Nb_2S_2C. The highest degree of catalytic activity was demonstrated by the S top in Nb_2S_2C, which had the lowest overpotential (η_{ORR} = 1.74 V) and optimal reaction energy of all the other systems.

3.2. Structural features, electronic properties, and OER & ORR activity of TM anchored Nb_2S_2C

Fig. 2 depicts the OER along with ORR process as well as the three intermediates that are connected to the TMs: OH*, O*, and OOH*. The adsorption structures of Nb_2S_2C anchored by X (X = Rh, Cd, Ir, Cu, and Pt) in conjunction with the intermediates (OH*, O*, and OOH*) are displayed in Fig. 2. In this work, we additionally examined the complete OER process, including intermediates involving O*, OH*, and OOH* atop the TM, as the literature research indicates that O adsorption isn't a reliable indicator of OER reactions. Fig. 2 depicts the OER along with ORR process as well as the three intermediates that are connected to the TMs: OH*, O*, and OOH*. The lattice properties are minimally altered by the addition of transition metals, depending on the dopant. For Pt, Ir, Cu, Cd, and Rh doping, the corresponding lattice parameters are 9.792, 9.791, 9.777, 9.790, and 9.771 Å. Accordingly, the lattice stress is −0.076%, −0.066%, −0.22%, −0.082%, and −0.281%. The doped systems maintain structural integrity, with minor modifications based on the atomic radius and bonding properties of the dopant, as evidenced by the observed modest contraction in lattice parameters. These modifications demonstrate how the dopant's size and liaison with the Nb_2S_2C lattice impact the outcomes. This allows one to better understand the mechanism as well as assess the role of X-anchoring (X = Rh, Cd, Ir, Cu, and Pt) in the OER reaction's over potential measurement. The structure is found to be immutable after the intermediates are adsorbed, *i.e.*, the intermediates are still attached to dopants of the TM–Nb_2S_2C, system. In the SI (Fig. S1), we present the optimized structures of transition metal anchored Nb_2S_2C along with the intermediate models.

When evaluating the reusability and structural stability of single-atom catalysts (SACs), the binding energy (E_b) serves

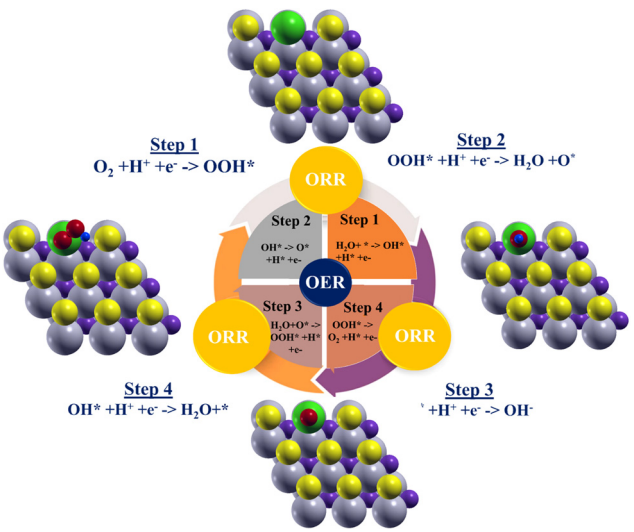

Fig. 2 Combined schematic of OER and ORR processes on Nb_2S_2C, illustrating the sequential reaction steps and their adsorbed intermediates: grey Nb; yellow S; purple C; green TM; red O; navy blue H.

as a key descriptor. It was calculated using the following relation:

$$E_b = E(TM/Nb_2S_2C) - E(Nb_2S_2C) - E(TM) \quad (1)$$

where E(TM) denotes the total energy of the isolated TM atom, and E(TM/Nb_2S_2C) represents the total energy of the Nb_2S_2C monolayer with an anchored TM atom. Using eqn (1), the calculated binding energies for Pt, Cu, Ir, Cd, and Rh anchored on Nb_2S_2C were found to be −5.43, −3.50, −5.61, −1.51, and −4.73 eV, respectively. The consistently negative values of E_b confirm that the Nb_2S_2C substrate provides strong affinity and robust anchoring sites for these TMs, underscoring their structural stability and suitability for catalytic applications.

By individually attaching the OH*, O*, and OOH* species to TM anchored Nb_2S_2C surfaces, the adsorption energies of these species are determined, accompanied by geometry relaxation. The adsorption arrangement of OH*, O*, and OOH* intermediates with respect to TM anchored Nb_2S_2C is depicted in Fig. 2. The calculated reaction energy associated with each oxygen evolution process occurring at the active sites of Nb_2S_2C is shown in Fig. 3. The kinetic transformations of the TM anchored Nb_2S_2C systems are as follows: Cd (2^{nd} step: from OH* to O*), Ir, Pt, Cu, and Rh (3^{rd} step: from O* to OOH*). The substitution of Pt enhances the contact that exists between the O* and the catalyst surface, thereby boosting the activity of the OER. The maximal reaction energy for every system was calculated to make comparisons easier. The energies associated with the following systems were determined to be 2.68, 2.15, 2.21, 1.85, and 1.55 eV. Cd, Cu, Ir, Rh, and Pt–Nb_2S_2C are the successive orders in which the OER activity shows a reduction in overpotential values but an increase in catalytic activity. Among all other systems, the Pt top in Pt–Nb_2S_2C was shown to have the highest amount of catalytic activity, with a minimal overpotential and the most reaction energy (η_{OER} = 0.32 V).

A common descriptor for determining the strength of adsorbate and catalyst interactions on various surfaces is the d-band centre. The d-band centre is found in the manner described below:

$$\varepsilon_d = \frac{\int_{-\alpha}^{\alpha} p(\varepsilon)\varepsilon d\varepsilon}{\int_{-\alpha}^{\alpha} p(\varepsilon) d\varepsilon} \quad (2)$$

The density of states is represented by the symbol ρ, while the energy breadth of the d orbital is represented by ε_d.[19] The d orbital associated with the metal atom significantly influences the electronic properties present at the surface of the transition metal (TM) catalyst. To gain detailed insight into the nature of the bonding behaviour among the various chemical species participating in the associative reaction step, an analysis of the projected density of states (PDOS) along with the evaluation of the d-band centre (ε_d) corresponding to the adsorption of hydroxyl (OH), atomic oxygen (O), and hydroperoxyl (OOH) on the Pt-doped Nb_2S_2C surface was conducted, as depicted in Fig. 4 (panels a–c). The data reveal a clear hybridization between Pt–Nb_2S_2C and the associated intermediates.

Upon adsorption of the intermediates, the d-band centre in each studied model shifts away from the reference point of −0.52 eV, moving in a direction opposite to the Fermi level. This shift is a consequence of the electron redistribution

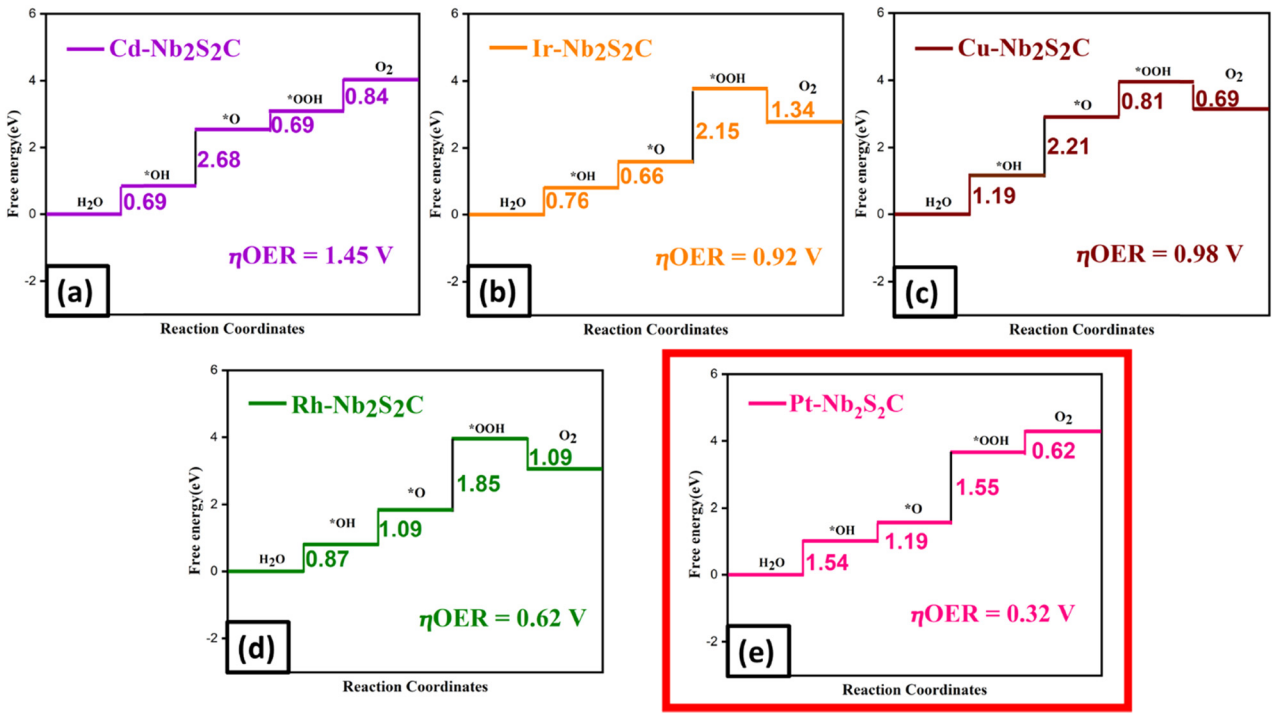

Fig. 3 Gibbs free-energy diagrams for the OER pathways on (a) Cd–Nb_2S_2C, (b) Ir–Nb_2S_2C, (c) Cu–Nb_2S_2C, (d) Rh–Nb_2S_2C, and (e) Pt–Nb_2S_2C. The black marker in each profile highlights the rate-limiting step with the highest energy barrier.

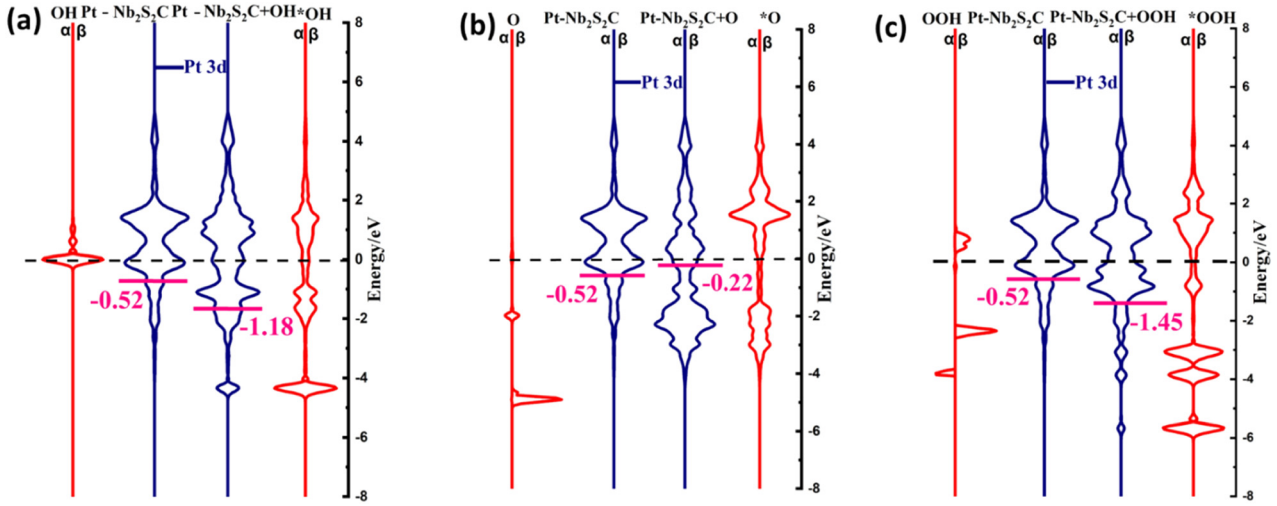

Fig. 4 Projected density of states (PDOS) for Pt–Nb_2S_2C, showing (a)–(c) the Pt 3d states (blue) and the 2p states of O, OH, and OOH before and after adsorption (red). The d-band centre of the Pt–Nb_2S_2C substrate, prior to and following intermediate adsorption, is indicated by the pink line.

occurring as a result of the hybridization between the d orbitals of Pt–Nb_2S_2C and the sp orbitals of the adsorbed species. The metal atom undergoes electron loss to establish a balanced and effective chemical bond with the intermediate. Additionally, the increased occupancy of antibonding orbitals, a direct outcome of the hybridization between the metal's d band and the s/p orbitals of the adsorbate, is represented by a lower and more optimally located d-band centre. This behaviour correlates with a decreased activation energy for the dissociation of reactants, thereby facilitating the desorption of intermediates during the overall catalytic process.

Furthermore, when hydrogen (H) and *adsorbed hydroxyl (OH) interact to form adsorbed oxygen (*O), the d-band centre rises by approximately 0.96 eV, indicating the possibility that a higher number of antibonding orbitals become populated in the presence of hydrogen. When –OH is connected to the *O species, further electron depletion takes place due to ongoing orbital hybridization. The adsorption of the *OOH species, which possesses an increased density of electronic states near the Fermi level, leads to a further lowering of the d-band centre.

Altogether, these findings clearly indicate that the oxygen evolution reaction (OER) performance of the Pt-doped Nb_2S_2C catalyst system is intricately dependent on both the electronic characteristics of the metal and the local electronic environment. The bonding strength between the adsorbed intermediates and the catalyst's surface directly influences the overall efficiency of the OER process. Moreover, the extent of electron transfer observed is closely linked to the strength and nature of the chemical bonding involved in each intermediate interaction. Table S2 offers an alternative method of understanding, in which the bond length is used to represent the electron cloud of the two elements. In Pt–Nb_2S_2C + OH, the bond lengths in between Pt and O and O to H are 1.79 and 0.97 Å, respectively, according to Table S2. In a similar vein the bond lengths that exist between Pt–O, O–O, and O–H are 2.00, 1.43, and 0.98 Å, respectively, and the overall bond length of Pt–Nb_2S_2C + OOH is 4.41 Å.

A series of Gibbs free energy diagrams appertaining to the ORR drill are shown in Fig. 5. The adsorbed hydroxyl group (OH*) interacts with another proton (H^+) and electron (e^-) to form a water molecule (H_2O) in the fourth phase, which uses the most energy throughout the entire ORR activity. This water molecule subsequently desorbs from the surface. In the case of Rh top in Nb_2S_2C, the ΔG_d value observed is −0.87 eV. The foremost energy-intensive process for Pt–Nb_2S_2C, and Cu–Nb_2S_2C is the first step of O_2 with a H^+ and an e^- to produce the OOH* on the catalyst surface. The corresponding ΔG_a values for these processes are −0.62 and −0.69 eV. The energy-intensive stage for Cd–Nb_2S_2C and Ir–Nb_2S_2C is the second phase, in which adsorbed OOH* undergoes a reaction with another H^+ and e^-, resulting in the formation of an adsorbed O* and H_2O. Thirdly, the adsorbed oxygen atom (O*) undergoes a reaction with a proton and an electron on the catalyst surface to produce a hydroxyl group with ΔG_b values of −0.69 and −0.66 eV. The fact that the Rh top in Nb_2S_2C has the lowest possible overpotential (η_{ORR} = 0.35 V) for the ORR out of all the TM–Nb_2S_2C materials that have been investigated is very significant [Fig. 5(d)]. Moreover, as illustrated in Fig. 5, the overpotentials of other transition metal doped Nb_2S_2C for the ORR were calculated.

The results (η_{ORR} = 4.28, 1.74, and 4.64 V for Nb, S, and C top in Nb_2S_2C, respectively) demonstrate that the addition of Cd, Ir, Cu, Pt, and Rh greatly improves the ORR efficiency of pristine Nb_2S_2C. Accordingly, the activity of the ORR increases in the following sequence: Pt, Ir, Cd, Cu, and Rh top on Nb_2S_2C. The Rh top in Nb_2S_2C was found to have the lowest overpotential (η_{ORR} = 0.35 V) and the shortest optimum reaction energy among all the other systems, evincing the highest level of catalytic activity. Consequently, in addition to Rh top's ORR activity in Nb_2S_2C, Pt top exhibits competent OER catalytic activity.

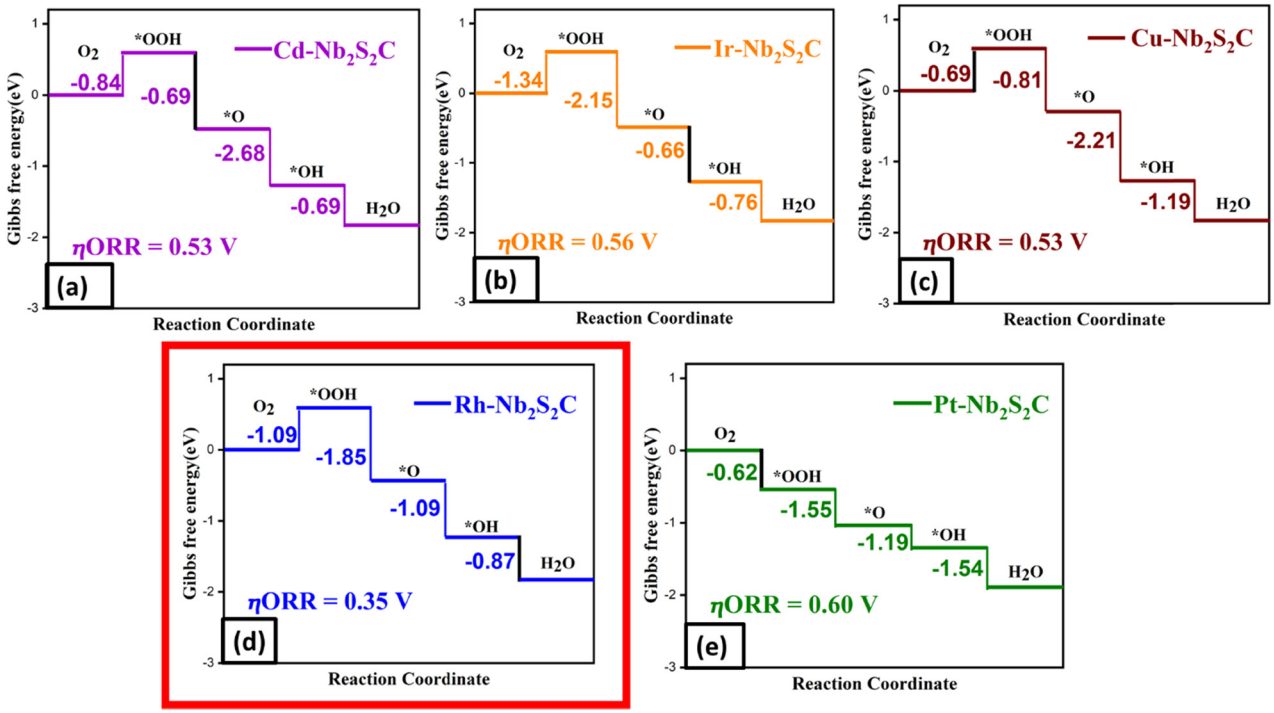

Fig. 5 Gibbs free-energy diagrams for the ORR pathways on (a) Cd–Nb_2S_2C, (b) Ir–Nb_2S_2C, (c) Cu–Nb_2S_2C, (d) Rh–Nb_2S_2C, and (e) Pt–Nb_2S_2C. The black marker highlights the rate-limiting step with the highest energy barrier in each pathway.

The dissociation of OOH is an essential initial stage in the ORR process that establishes the reaction pathway's overall efficiency. The breaking of the O–O bond in OOH is crucial for the synthesis of two distinct intermediates (O and OH), which ultimately result in the formation of water, especially for the four-electron ORR process. Therefore, examining the OOH dissociation helps determine if the catalyst can support the ORR and offers important insights into the activation energy needed for O–O bond breaking. Other processes, such as O_2 adsorption, protonation to produce OOH, and H_2O desorption, are either known to happen readily on Ru based systems or are comparatively simple. As a result, we concentrated our NEB calculations on OOH dissociation, the phase that requires the greatest energy and limits pace. Density functional theory (DFT) calculated free energy diagrams reveal that the dissociation of OH on the metal centre of single-atom catalysts (SACs) is the most endothermic elementary step for most SAC systems. A widely accepted strategy to improve the oxygen reduction reaction (ORR) efficiency is to reduce the adsorption strength of OH on the metal centre. While the activation energy for OOH dissociation also plays a critical role, Wang and co-workers have identified OOH dissociation as the kinetically dominant step in the ORR pathway on SACs.

According to the energy profile obtained from nudged elastic band (NEB) calculations, the activation barrier for OOH dissociation is approximately 2.25 eV. On Rh-doped Nb_2S_2C, this dissociation process is thermodynamically favourable. After overcoming the energy barrier, the system reaches a final state that is 0.80 eV lower in energy than the initial configuration (see Fig. 6), confirming the stability of the resulting OH and O adsorbates. To contextualize our results, we compare them with the well-established FeN_4@graphene system reported by Kattel and Wang.[28] In their study, the minimum-energy pathway similarly identifies OOH dissociation as the decisive step controlling ORR kinetics. Their NEB energy profile shows that the transition state lies significantly above the initial state, indicating that substantial activation energy is required to cleave the O–O bond consistent with our

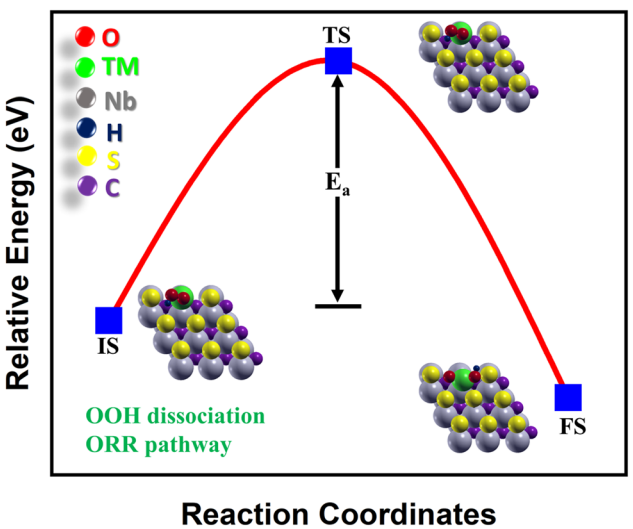

Fig. 6 Minimum-energy pathway for the Tafel reaction on Rh–Nb_2S_2C, with the atomic structures of the initial (IS), intermediate (IM), and final (FS) states shown in the insets.

findings for Rh@Nb_2S_2C. Moreover, the FeN_4 system demonstrates strong stabilization of the final O and OH intermediates after surmounting the energy barrier, analogous to the ~0.80 eV stabilization observed in our catalyst. This comparison underscores that OOH dissociation constitutes the key kinetic bottleneck not only in classical FeN_4 SACs but also in our Rh anchored Nb_2S_2C system. Our findings align well with the FeN_4 reference system, reinforcing the proposed mechanism and emphasizing that efficient OOH dissociation is key to achieving high ORR activity in SAC-based catalysts. OOH dissociation is a crucial initial step in the ORR mechanism, as it determines the overall efficiency of the reaction pathway. The cleavage of the O–O bond in the OOH intermediate yields two distinct species O and OH, which are necessary precursors for the eventual formation of water, particularly in the four-electron ORR route. Thus, evaluating OOH dissociation provides essential insight into both the catalytic feasibility and the activation energy required for effective O–O bond cleavage. Other ORR related processes, such as O_2 adsorption, protonation to form OOH, and H_2O desorption, are generally facile on Ru-based catalysts or involve comparatively low energy barriers. Given that OOH dissociation is both energetically demanding and the rate-limiting step, it was therefore the primary focus of our NEB calculations.[20–22]

In OER/ORR processes, the relationship between the Gibbs free energy of three intermediates (ΔG_{OH}, ΔG_O, and ΔG_{OOH}) tends to be used to characterize the overpotential as well as the strength of the interaction between intermediates and active atoms. In Fig. 7(a and b), the scaling tandem among the Gibbs free energies of ΔG_{OH} and ΔG_{OOH}, as well as the Gibbs free energies of ΔG_O and ΔG_{OH} of the examined TM doped Nb_2S_2C, is visualised. The formula for the regression analysis may be formulated as $\Delta G_{OOH} = \Delta G_{OH} + 3.17$, with a coefficient determination (R^2) of 0.99, indicating a strong agreement with other catalysts for the OER and ORR. Nevertheless, it seems that the linear equation explaining the relationship between ΔG_O and ΔG_{OH} accurately represents all the data, as shown by $\Delta G_O = 1.42\ \Delta G_{OH} + 0.52$ with an R^2 value of 0.70. In accordance with previous research, a slope of 1 for

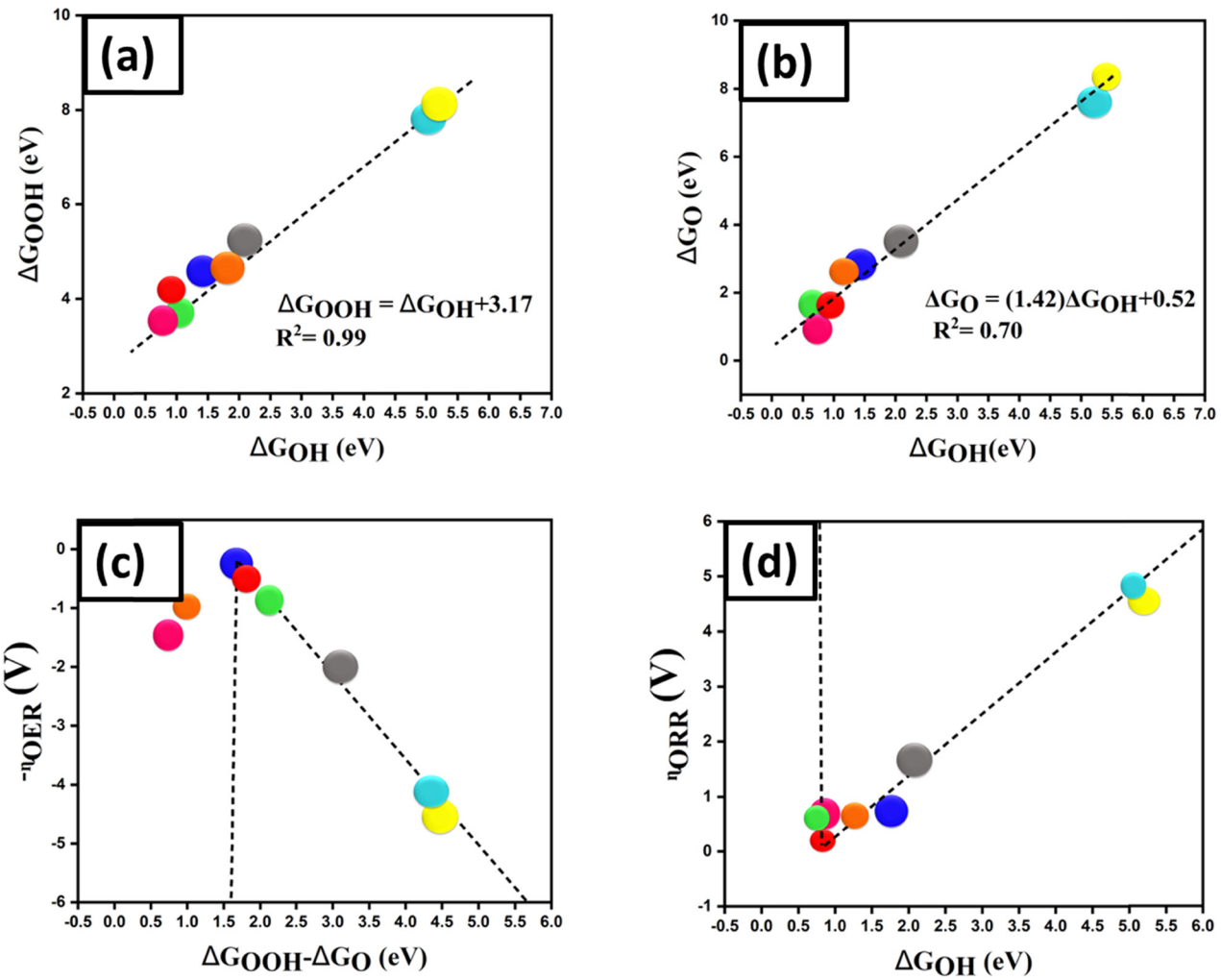

Fig. 7 (a) Scaling relation between ΔG_{OH} and ΔG_{OOH} for pristine Nb_2S_2C and TM–Nb_2S_2C. (b) Scaling relation between ΔG_{OH} and ΔG_O. (c) Volcano plot of $-\eta_{OER}$ *versus* $\Delta G_{OOH} - \Delta G_O$. (d) Inverse volcano plot of η_{ORR} and ΔG_{OH}. Color scheme: grey (S–Nb_2S_2C), yellow (Nb–Nb_2S_2C), light blue (C–Nb_2S_2C), red (Rh–Nb_2S_2C), pink (Cd–Nb_2S_2C), green (Ir–Nb_2S_2C), orange (Cu–Nb_2S_2C), blue (Pt–Nb_2S_2C).

ΔG_{OOH} + 3.17 suggests that OH* and OOH* have akin bond orders and are each bound by a single bond to TM atoms.[23]

Given that the potential determining stages (PDS) of the OER for both pristine and TM doped Nb_2S_2C primarily occur during the ΔG_3 (OOH* to O*) transition, the overpotential η_{OER} may be calculated by comparing the potentials of ΔG_{OOH} and ΔG_O. The $\Delta G_{OOH} - \Delta G_O$ descriptor was used to characterize η_{OER}, and a volcano curve can be graphed (see Fig. 7(c)). Hence, the presence of the Pt top in Nb_2S_2C at the summit of the volcano confirms the superior electrocatalytic activities. In ORR processes, the PDS of both pristine and TM-doped Nb_2S_2C is mostly observed at the third step (O* to OH*) and fourth step (OH* to H_2O). Next, we opted for ΔG_{OH} as a descriptor for η_{ORR}, allowing for the plotting of an inverted volcano (Fig. 7(d)). Similarly, the most effective ORR electrocatalyst is the Rh doped Nb_2S_2C found at the pinnacle of the volcano.

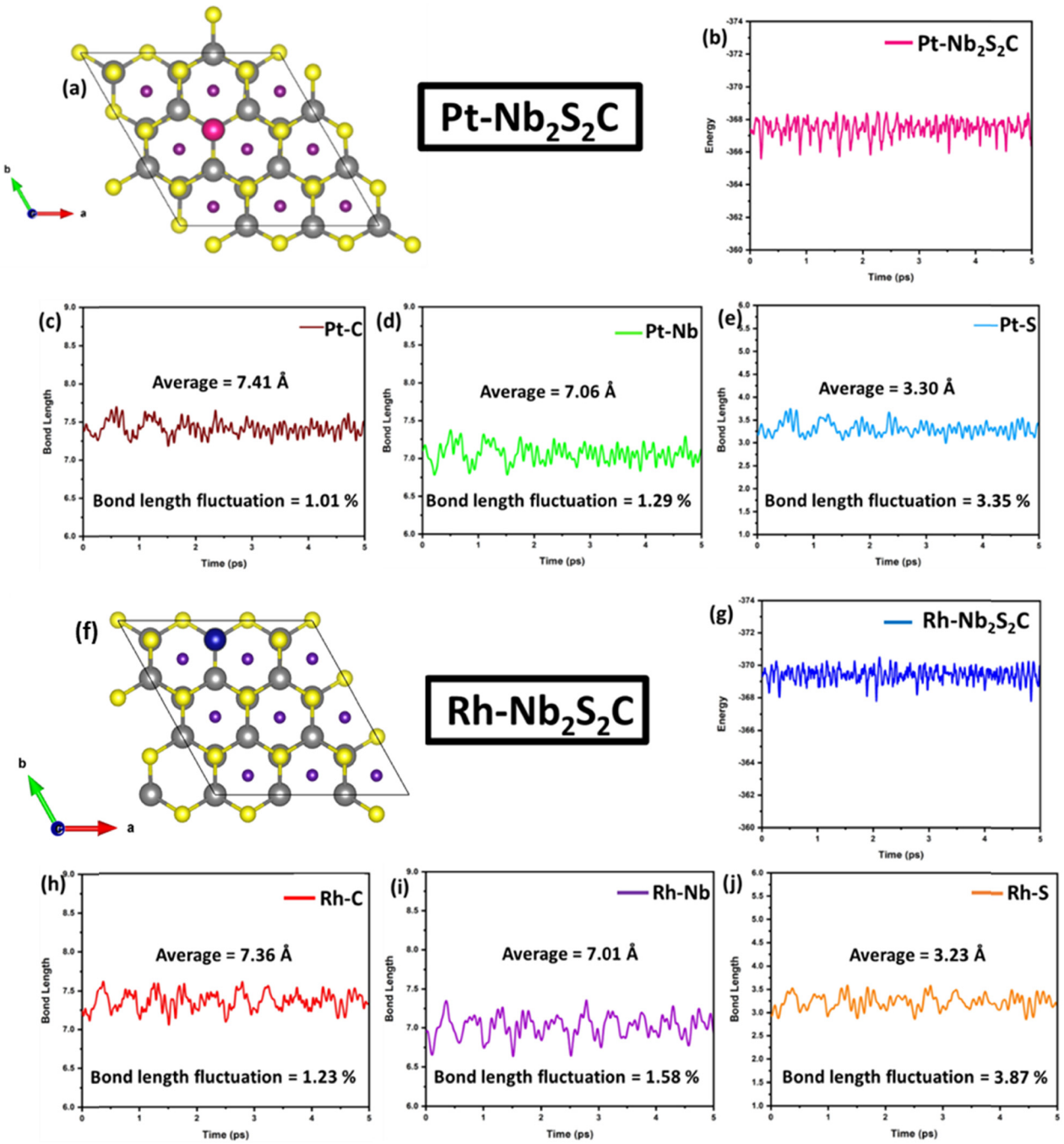

Fig. 8 (a) and (f) MD snapshots of Pt- and Rh-anchored Nb_2S_2C at 300 K after 5 ps. (b) and (g) Total energy fluctuations during the 300 K MD simulations for the Pt- and Rh-anchored systems. (c)–(e) Bond-length fluctuations of Pt–C, Pt–Nb, and Pt–S pairs. (h)–(j) Bond-length fluctuations of Rh–C, Rh–Nb, and Rh–S pairs, all evaluated over 5 ps at 300 K.

3.3. Thermal and structural integrity of Pt and Rh anchored Nb_2S_2C using molecular dynamics simulations

Because standard DFT calculations are performed at 0 K, they may not accurately reflect catalyst structures at ambient or elevated temperatures. For catalytic processes such as the oxygen evolution (OER) and oxygen reduction (ORR) reactions, the substrate must maintain its structural integrity during reactant desorption and at room temperature to be reusable in subsequent cycles.[27] To assess the thermal stability of Pt and Rh anchored Nb_2S_2C, *ab initio* MD simulations were conducted in two stages. In the first stage (NVE ensemble), the system temperature was gradually raised to 300 K over 5 ps (with a 1 fs time step). In the second stage (NVT ensemble), a Nosé–Hoover thermostat was used to equilibrate the system at 300 K. These simulations were performed using the VASP code. The resulting bond lengths, energy fluctuations, and MD snapshots indicate that the Pt and Rh atoms remain bonded to the Nb_2S_2C lattice at 300 K, and the overall structure shows minimal deformation under these conditions [see Fig. 8(a and f)]. Consequently, Pt- and Rh-anchored Nb_2S_2C catalysts exhibit robust structural stability, suggesting promising OER and ORR performance and making them attractive for renewable energy applications.

At an equilibrium temperature of 300 K, MD simulations have shown the bond length fluctuation of Pt–C (= 7.41 Å), Pt–Nb (= 7.06 Å), Pt–S (= 3.30 Å), Rh–C (= 7.36 Å), Rh–Nb (= 7.01 Å), and Rh–S (= 3.23 Å) atomic pairs during a period of 5 ps (Fig. 8(c, d, e, h, i, j)). According to the data, these atomic pairs' net bond length fluctuation is 1.01%, 1.29%, 3.35%, 1.23%, 1.58%, and 3.87%. No indications of degradation were seen in the Pt and Rh–Nb_2S_2C framework, hence affirming the structure's thermodynamic stability at elevated temperatures.

In Table 1, the pristine Nb_2S_2C system, TM-anchored Nb_2S_2C, from our research work, and previously published nanomaterials are thoroughly compared. Thus, as evidenced by the results from Fig. 3 and 5, it can be seen that Pt and Rh in Nb_2S_2C exhibit higher OER and ORR activity than both the pristine and other doped versions of transition metals, such as Cd, Cu, and Ir.

There are several synergistic mechanisms that contribute to the decrease in OER and ORR overpotentials in Pt and Rh-doped Nb_2S_2C. In order to optimize the adsorption strength of important intermediates (O*, OH*, OOH* for OER and O_2*, OOH*, OH* for ORR), metal doping first shifts the d-band centre closer to the Fermi level, tuning the electronic structure and improving the reaction kinetics. Furthermore, Pt and Rh promote charge redistribution, reducing energy barriers and enhancing the effectiveness of charge transfer at the active sites. Energy losses are mitigated by stabilizing advantageous adsorption configurations by the alteration of the local coordination environment introduced by doping. Furthermore, Pt and Rh's potent catalytic properties guarantee effective electron transfer pathways, enhancing intrinsic activity. Together, these actions work in concert to reduce the overpotential and improve Nb_2S_2C's catalytic activity. We may infer that the TM anchored Nb_2S_2C could be a viable bifunctional electrocatalyst for the OER, and ORR because the Pt doped Nb_2S_2C, and the Rh doped Nb_2S_2C have appealing lower over potential for the OER and ORR activity.

Table 1 The comparison of calculated η of TM–Nb_2S_2C with previous reported nanomaterials, respectively

System	η (V)	Ref.
Ni_2B_5	0.39 (OER)	24
	0.62 (ORR)	24
NiC_3	0.60 (OER)	24
	0.31 (ORR)	24
Pd@$PtSe_2$	0.31 (OER)	25
	0.43 (ORR)	25
Cu–C_3N_2	0.53 (OER)	26
	0.52 (ORR)	26
Rh–Nb_2S_2C	0.35 (ORR)	Present work
Pt–Nb_2S_2C	0.32 (OER)	Present work

4. Conclusion

In this study, dispersion-corrected density functional theory (DFT) calculations were employed to investigate the bifunctional electrocatalytic activity of pristine and transition metal (TM) doped Nb_2S_2C monolayers toward the oxygen evolution reaction (OER) and oxygen reduction reaction (ORR). The results demonstrate that TM doping significantly enhances the catalytic performance by modulating the electronic structure and optimizing the adsorption energies of key intermediates. Among all dopants considered, Pt- and Rh-doped Nb_2S_2C exhibit the most promising bifunctional behaviour, with low overpotentials of 0.32 V for the OER and 0.35 V for the ORR, respectively. Electronic structure analyses reveal that TM incorporation tunes the d-band centre and facilitates efficient charge transfer between the active sites and adsorbed species, thereby lowering the activation barriers and improving the reaction kinetics. Nudged elastic band (NEB) calculations identify the OOH dissociation step as the rate-determining step in the four-electron ORR pathway for Rh–Nb_2S_2C, with an activation energy of 2.25 eV. Moreover, *ab initio* molecular dynamics (AIMD) simulations confirm the thermal and structural stability of Pt and Rh-doped Nb_2S_2C at 300 K, reinforcing their suitability for practical electrocatalytic applications. Overall, this work provides a comprehensive theoretical framework for understanding and designing high-performance Nb_2S_2C-based electrocatalysts. The superior activity and stability of Pt- and Rh-doped Nb_2S_2C underscore their potential as cost-effective and durable bifunctional catalysts for next-generation clean energy systems, including fuel cells, metal–air batteries, and water-splitting devices.

Conflicts of interest

The authors declare that they have no discernible competing financial interests or personal relationships that would have influenced the results of this study.

Data availability

All data supporting this study are included within the article and the supplementary information (SI), and are available from the corresponding author upon reasonable request. Supplementary information is available. See DOI: https://doi.org/10.1039/d6ma00002a.

The authors will make the data publicly available in an appropriate repository upon publication.

Acknowledgements

KSJ expresses profound gratitude to University Grants Commission (UGC) for administering the Savitribai Jyotirao Phule Fellowship for Single Girl Child (SJSGC). The authors highly acknowledge Charotar University of Science and Technology for providing computational facilities (PARAM Shavak and VISHNU cluster). The authors acknowledge BARC's Supercomputing facility where part of the simulations were carried out.

References

1 K. Zhang, Z. Wu, Z. Yang, J. Sun, C. Ma, S. Luo, W. Li and S. Liu, *J. Energy Storage*, 2024, **95**, 112395.
2 Z. A. Sheikh, D. Vikraman, H. Kim, S. Aftab, S. F. Shaikh, F. Shahzad, J. Jung, H. S. Kim, S. Hussain and D. K. Kim, *J. Energy Storage*, 2024, **81**, 110342.
3 K. S. Joseph, B. Chakraborty and S. Dabhi, *Surf. Interfaces*, 2024, **56**, 105561.
4 K. S. Joseph and S. Dabhi, *Electrochim. Acta*, 2024, **505**, 144968.
5 K. S. Joseph, S. Dabhi and B. Chakraborty, *2D Mater. Electrochem. Sensors*, 2023, 133–158.
6 M. N. Braud, M. Couzi, N. B. Chanh, C. Courseille, B. Gallois, C. Hauw and A. Meresse, *J. Phys.: Condens. Matter*, 1990, **2**, 8209.
7 H. Nowotny, H. Boller and O. Beckmann, *J. Solid State Chem.*, 1970, **2**, 462–471.
8 H. Boller and K. Hiebl, *J. Alloys Compd.*, 1992, **183**, 438–443.
9 K. Sakamaki, H. Wada, H. Nozaki, Y. Onuki and M. Kawai, *Solid State Commun.*, 2001, **118**, 113–118.
10 K. Belay Ibrahim, T. Ahmed Shifa, S. Zorzi, M. Getaye Sendeku, E. Moretti and A. Vomiero, *Prog. Mater. Sci.*, 2024, **144**, 101287.
11 A. Majed, M. Kothakonda, F. Wang, E. N. Tseng, K. Prenger, X. Zhang, P. O. Å. Persson, J. Wei, J. Sun and M. Naguib, *Adv. Mater.*, 2022, **34**, 2200574.
12 M. Li, T. Li and Y. Jing, *ACS Omega*, 2023, **8**, 31051–31059.
13 K. H. Yeoh, Y. H. R. Chang, K. H. Chew, J. Jiang, T. L. Yoon, D. S. Ong and B. T. Goh, *Langmuir*, 2023, **40**, 3569–3576.
14 S. Lakshmy, N. Kalarikkal and B. Chakraborty, *Langmuir*, 2024, **40**, 13819–13833.
15 P. Giannozzi, *et al.*, *J. Phys.: Condens. Matter*, 2009, **21**, 395502.
16 J. P. Perdew and K. Burke, *Phys. Rev. B: Condens. Matter Mater. Phys.*, 1996, **54**, 16533–16539.
17 S. Grimme, *J. Comput. Chem.*, 2006, **27**, 1787–1799.
18 F. Xu, Z. Gao, Z. Ge, H. Ma, H. Ren, H. Zhu, Y. Chi, W. Guo and W. Zhao, *Phys. Chem. Chem. Phys.*, 2023, **25**, 17508–17514.
19 G. Hou, Y. Song, X. Ma, F. Chu, M. Wu, D. Wang, J. Wu, Y. Qi, C. Wu and M. Xiong, *J. Mol. Graphics Modell.*, 2022, **111**, 108101.
20 L. Li, B. Huang, X. Tang, Y. Hong, W. Zhai, T. Hu, K. Yuan and Y. Chen, *Adv. Funct. Mater.*, 2021, **31**, 2103857.
21 K. Liu, G. Wu and G. Wang, *J. Phys. Chem. C*, 2017, **121**, 11319–11324.
22 S. Kattel and G. Wang, *J. Phys. Chem. Lett.*, 2014, **5**, 452–456.
23 Z. Xue, X. Zhang, J. Qin and R. Liu, *J. Energy Chem.*, 2021, **55**, 437–443.
24 Y. Wei, H. Huang, F. Gao and G. Jiang, *Int. J. Hydrogen Energy*, 2023, **48**, 4242–4252.
25 S. Yue, D. Li, A. Zhang, Y. Yan, H. Yan, Z. Feng and W. Wang, *J. Mater. Chem. A*, 2024, **12**, 5451–5463.
26 J. Zhang, L. Ju, Z. Tang, S. Zhang, G. Zhang and W. Wang, *ACS Appl. Nano Mater.*, 2024, **7**, 24653.
27 K. S. Joseph, B. Chakraborty and S. Dabhi, *Phys. Chem. Chem. Phys.*, 2025, **27**, 21739–21751.
28 S. Kattel and G. Wang, *J. Phys. Chem. Lett.*, 2014, **5**, 452–456.